



**HAL**  
open science

## Carburization of austenitic and ferritic stainless steels in liquid sodium: Comparison between experimental observations and simulations

Marie Michelle Romedenne, Fabien Rouillard, Didier Hamon, Benoît Malard,  
Daniel Monceau

### ► To cite this version:

Marie Michelle Romedenne, Fabien Rouillard, Didier Hamon, Benoît Malard, Daniel Monceau. Carburization of austenitic and ferritic stainless steels in liquid sodium: Comparison between experimental observations and simulations. *Corrosion Science*, 2019, 159, pp.108147. 10.1016/j.corsci.2019.108147 . hal-02388742

**HAL Id: hal-02388742**

**<https://hal.science/hal-02388742>**

Submitted on 2 Dec 2019

**HAL** is a multi-disciplinary open access archive for the deposit and dissemination of scientific research documents, whether they are published or not. The documents may come from teaching and research institutions in France or abroad, or from public or private research centers.

L'archive ouverte pluridisciplinaire **HAL**, est destinée au dépôt et à la diffusion de documents scientifiques de niveau recherche, publiés ou non, émanant des établissements d'enseignement et de recherche français ou étrangers, des laboratoires publics ou privés.



## Open Archive Toulouse Archive Ouverte (OATAO)

OATAO is an open access repository that collects the work of Toulouse researchers and makes it freely available over the web where possible

This is a Publisher's version published in: <https://oatao.univ-toulouse.fr/cgi/users/home?screen=EPrint::View&eprintid=25152>

**Official URL:** <https://www-sciencedirect-com.gorgone.univ-toulouse.fr/science/article/pii/S0010938X19310169>

**To cite this version:** Romedenne, M. and Rouillard, F. and Hamon, D. and Malard, B. and Monceau, D. *Carburization of austenitic and ferritic stainless steels in liquid sodium: Comparison between experimental observations and simulations*. (2019) Corrosion Science, 159. 108147. ISSN 0010938X

Any correspondence concerning this service should be sent to the repository administrator: [tech-oatao@listes-diff.inp-toulouse.fr](mailto:tech-oatao@listes-diff.inp-toulouse.fr)

# Carburization of austenitic and ferritic stainless steels in liquid sodium: Comparison between experimental observations and simulations

M. Romedenne<sup>a,\*</sup>, F. Rouillard<sup>b</sup>, D. Hamon<sup>c</sup>, B. Malard<sup>d</sup>, D. Monceau<sup>d</sup>

<sup>a</sup> *Materials Science and Technology Division, Oak Ridge National Laboratory, Oak Ridge, TN 37831-6156, USA*

<sup>b</sup> *Den-SERVICE de la Corrosion et du Comportement des Matériaux dans leur Environnement (SCCME), CEA, Université Paris-Saclay, F-91191 Gif-sur-Yvette, France*

<sup>c</sup> *Den-SERVICE de Recherches Métallurgiques Appliquées (SRMA), CEA, Université Paris-Saclay, F-91191 Gif-sur-Yvette, France*

<sup>d</sup> *CIRIMAT, Université de Toulouse, CNRS, INPT, UPS, ENSIACET 4, allée Emile Monso BP-44362, 31030 Toulouse cedex 4, France*

## A B S T R A C T

Three steels were exposed in carburizing sodium at 600 and 650 °C. The kinetics and extent of carburization were characterized. Numerical simulations using the coupled thermodynamic-kinetic modeling software DICTRA were performed. It was proposed that the observed carbon diffusion profiles were induced by the combined diffusion of carbon in the grains and at grain boundaries coupled with the slow formation of carbides. The blocking effect of carbides on the carbon diffusion was observed to evolve as a function of time and microstructure. Acceptable agreement between experimental and simulated intragranular carbon profiles was achieved by optimizing the labyrinth factor and phases.

## 1. Introduction

In the framework of the development of a Sodium-cooled Fast nuclear Reactor (SFR) prototype for industrial demonstration called ASTRID (Advanced Sodium Technological Reactor for Industrial Demonstration), the French Alternative Energies and Atomic Energy Commission and its industrial partners have launched intensive research programs on several reactor components where improvements are needed. In particular, in the core of the reactor, the control rods are prone to carburization, a phenomenon responsible for their embrittlement and thus, reduced lifetime [1]. The nature and kinetics of carburization of steels in liquid sodium at 450–650 °C, where the activity of carbon in sodium is close to unity, were studied in the past. These studies led to the development of simplified carburization models predicting the evolution of the carburization kinetics of stainless steels in sodium [2–7]. In these approaches, apparent diffusion coefficients of carbon  $D_{app}$  were calculated by fitting the carbon concentration profiles with the usual solution of the Fick's second law [8]. In most of the studies, this parameter was neither clearly related to the diffusion of carbon in the matrix (ferrite or austenite) nor related to an effective grain boundary coefficient [2–6]. Only Dickson et al. [7] proposed a prediction of the carbon concentration profiles using two different apparent diffusion coefficients,  $D_{app}$ , one for the apparent diffusion of carbon in the grains and another one for the apparent grain boundary diffusion of carbon. In most of the cases,  $D_{app}$  was a fitted parameter

used to predict the maximum thickness affected by the carburization process. It is obvious that the maximum carburized thickness depends on the material (carbon diffusion coefficient in the matrix and at grain boundaries and the amount of precipitated phases (carbides)). As a consequence,  $D_{app}$  is strongly dependent on the nature of the steel. It cannot be used to predict the carburized thickness of another steel with a different chemical composition and microstructure. Thus, a more accurate lifetime model is needed.

In the present study, out-of-pile carburization experiments were performed in liquid sodium at 600 and 650 °C (maximum temperatures measured in the core). Three stainless steels grades coupons were exposed and their extent of carburization and kinetics were followed. Moreover, the carburization kinetics in liquid sodium was simulated using DICTRA-ThermoCalc software. DICTRA is a module of the commercial software ThermoCalc which allows simulations of diffusion controlled transformations in multi-component systems [9]. DICTRA is commonly used to simulate carburization or nitriding kinetics [10–14]. The first published DICTRA simulations, reported by A. Engström et al. [10], simulated the carburization behavior of Ni-Cr and Ni-Cr-Fe at 850 °C after 1000 h exposure under 10% CH<sub>4</sub> and  $a_C = 1$  and Fe-25Cr-20Ni alloys after carburization for 200 h at 1100 °C. They compared the results with literature data [15–17]. For the first set of experiments they simulated with reasonable accuracy the evolution of M<sub>3</sub>C<sub>2</sub>, M<sub>7</sub>C<sub>3</sub> and M<sub>23</sub>C<sub>6</sub> carbides and the carbon concentration profiles with  $a_C = 1$  as boundary condition and with a labyrinth factor equal to  $f^2$  (the meaning

of this parameter will be detailed later in the manuscript). For the second set of experiments, good agreement was achieved between the simulated and experimental observations assuming the formation of  $M_7C_3$  and  $M_{23}C_6$  carbides,  $f^2$  as labyrinth factor and an adjusted boundary condition at the gas-metal interface ( $a_C = 0.45$ ). Turpin et al. [11] compared the experimental and calculated carbon profiles of Fe-13Cr-5Co-3Ni-2Mo-0.07C grades exposed at 955 °C for 23, 53 and 145 min. The predicted carbon profiles agreed well with the experimental carbon concentration profiles using the measured experimental carbon concentration at the gas-metal interface and, again, a labyrinth factor equal to  $f^2$ . Garcia et al. well predicted nitriding of alloy W-Ti-Ta-Nb-Co-C at 1400 °C [13]. All the previous DICTRA simulations observed a good agreement with experimental observations at high temperatures ( $T > 850$  °C). Few DICTRA simulations were reported for the carburization of steels at lower temperatures ( $T < 850$  °C) [12,14]. Sudha et al. attempted modelling the carburization behavior of 316L(N) steel at 525 °C after 16,000 h exposure without a clear description of their procedure [12]. Finally, Rong et al. attempted to simulate a carburization process at low temperature for which the precipitation of chromium rich carbides was prevented. Although the carburization depth was in agreement with the experimental results, the predicted carbon concentration at the surface was not in accordance with the experimental value [14].

The purpose of the present study is twofold. First, the extent of carburization and kinetics of three steel grades exposed in carbon-saturated sodium at 600 and 650 °C are characterized. Second, the experimental results are compared with simulations using the DICTRA module in order to discuss the processes which control the kinetics. In that purpose, an accurate description of the carburized samples, was crucial for the comparison with the DICTRA simulations. Electron Probe MicroAnalysis (EPMA), Transmission Electron Microscopy (TEM) and X-Ray Synchrotron Diffraction (XRD) were used to thoroughly characterize the extent of carburization of the steels.

## 2. Materials and experimental procedure

### 2.1. Materials

Two austenitic steel grades, AIM1 (strain-hardened 25%) and 316L (solution-annealed), and one ferritic-martensitic steel, EM10 (strain-hardened 25%), were studied. Detailed chemical composition of the three steels is given in Table 1. The austenitic steels were constituted of relatively equiaxed grains with a grain size of 40 and 10  $\mu\text{m}$  for AIM1 and 316L respectively. The microstructure of the EM10 was formed of martensite laths of 0.3–0.4  $\mu\text{m}$  width.

### 2.2. Experimental procedure

The carburization experiments were performed in a mild steel crucible (iron containing 0.38 wt. % of carbon) filled with 2 liters of nuclear grade liquid sodium previously purified from oxygen (composition reported in Table 2) with the use of Zr foils. A carbon activity higher than unity ( $a_C > 1$ ) was obtained in the liquid sodium by the rapid dissolution of carbon from the crucible into the sodium. A carbon activity higher than unity can be achieved by the formation of  $\text{Fe}_3\text{C}$  considering the metastable Fe-C system. In liquid sodium, high carbon activities were measured where the formation of acetylide  $\text{Na}_2\text{C}_2$  in

**Table 2**

Composition of the nuclear grade sodium (industrial).

Na	Ca	Cl	Fe	K	O
99.95 wt. %	2 ppm	4 ppm	1 ppm	4 ppm	< 5 ppm

liquid sodium was observed [18,19].

Coupons of the three steels grades (20 mm  $\times$  20 mm  $\times$  1 mm) with as-received surface finish were cleaned in ethanol and weighed prior to exposure in high temperature liquid sodium. The specimens were exposed under two temperatures. The first experiment was performed at 600 °C for various exposure times up to 5000 h. In the second experiment the specimens were exposed at 650 °C for 200 h.

Specimens of 1 mm thickness were used to evaluate the carburization kinetics. Additional 150  $\mu\text{m}$  thick strips of the respective steel grades were simultaneously exposed under the same conditions to measure the value of the carbon concentration reached in the samples at thermodynamic equilibrium with the carbon activity in sodium. Weight gain measurements were carried out after 500 h, 1000 h, 3000 h and 5000 h after three cleaning steps in ethanol to remove all metallic sodium from the surface of the samples. The total carbon content of the specimens was measured by infrared-inductive carbon combustion. Then, cross sections were polished and etched with either di-ammonium persulfate (10 g  $(\text{NH}_4)_2\text{S}_2\text{O}_8$ , 100 mL water) or oxalic acid (10 g of  $\text{C}_2\text{H}_2\text{O}_4$ , 100 mL water, 6 volts) for metallographic examination.

The carbon concentration profiles within the depth of the samples were measured on unetched cross sections by EPMA (SX 100 CAMECA) operated at 15 kV and 20 nA using the phi-rho-z method. The analytical crystal for  $K\alpha$  C was LPC2. Band scan mode ( $2 \times 50 \mu\text{m}^2$ ) was used to average the carbon concentrations over several grains of the sample. Three quantitative profiles (step 4  $\mu\text{m}$ ) were realized in each sample and showed a relative deviation of 5%. The total carbon content deduced from the EPMA profiles was in accordance with the values obtained using carbon combustion analysis and in agreement with the mass gain measurements within  $\pm 5\%$  [20].

Transmission XRD was performed on the ID11 beamline at the European Synchrotron Radiation Facility (ESRF). A single-scan approach was used to evaluate the chemical and structural gradients within the cross section of the samples. The experimental set-up is represented in Fig. 1. Similar set-up and experiments have already been used to study the phase ratio and stress gradient in ferritic thin films with a 150 nm depth resolution [21], or to measure the lattice parameter evolution in  $\alpha$ -titanium alloy after oxidation (beam dimensions of 300  $\mu\text{m}$  length and 7  $\mu\text{m}$  height) [22]. The samples were illuminated at 65 keV with a beam of 5  $\mu\text{m}$  height in the y direction and 100 to 800  $\mu\text{m}$  length in the x direction. A large length (800  $\mu\text{m}$ ) was necessary to maximize the number of grains in the analyzed volume. Careful attention was given to align the beam parallel to the surface of the samples. For this purpose, the signal of a photodiode was used. Calibration of the distance between the sample and the detector and of the instrument resolution was performed using a standardized  $\text{CeO}_2$  powder (NIST 674b). The powder was inserted inside a capillary and glued above the middle of the sample. After integrating the data on the entire 2D diffractogram, the 1D data were analyzed using the Rietveld method within the MAUD software [23]. With this approach, the volume fractions of the phases and their lattice parameters were refined using a full pattern matching approach.

**Table 1**

Composition of studied alloys (in wt. %) analyzed by inductively coupled plasma-optical emission spectrometry (ICP-OES) and combustion analysis for carbon.

Composition	Cr	Ni	Mo	C	Ti	Mn	Co	Si	Cu	Al	Fe
AIM1 (wt. %)	14.35	14.05	1.40	0.09	0.36	1.40	0.02	0.73	0.12	0.015	Base
316L (wt. %)	16.55	10.52	2.05	0.03	–	1.55	0.12	0.18	0.24	0.022	Base
EM10 (wt. %)	8.95	0.42	0.82	0.10	0.013	0.45	0.03	0.33	0.015	0.096	Base

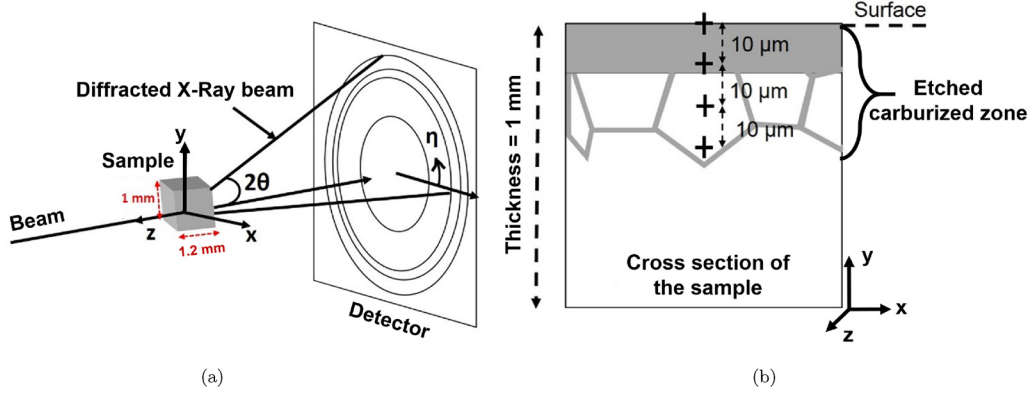


Fig. 1. (a) Experimental set-up of the X-ray diffraction measurements at ESRF. (b) Schematic view of a sample cross section annotated with the successive measurements.

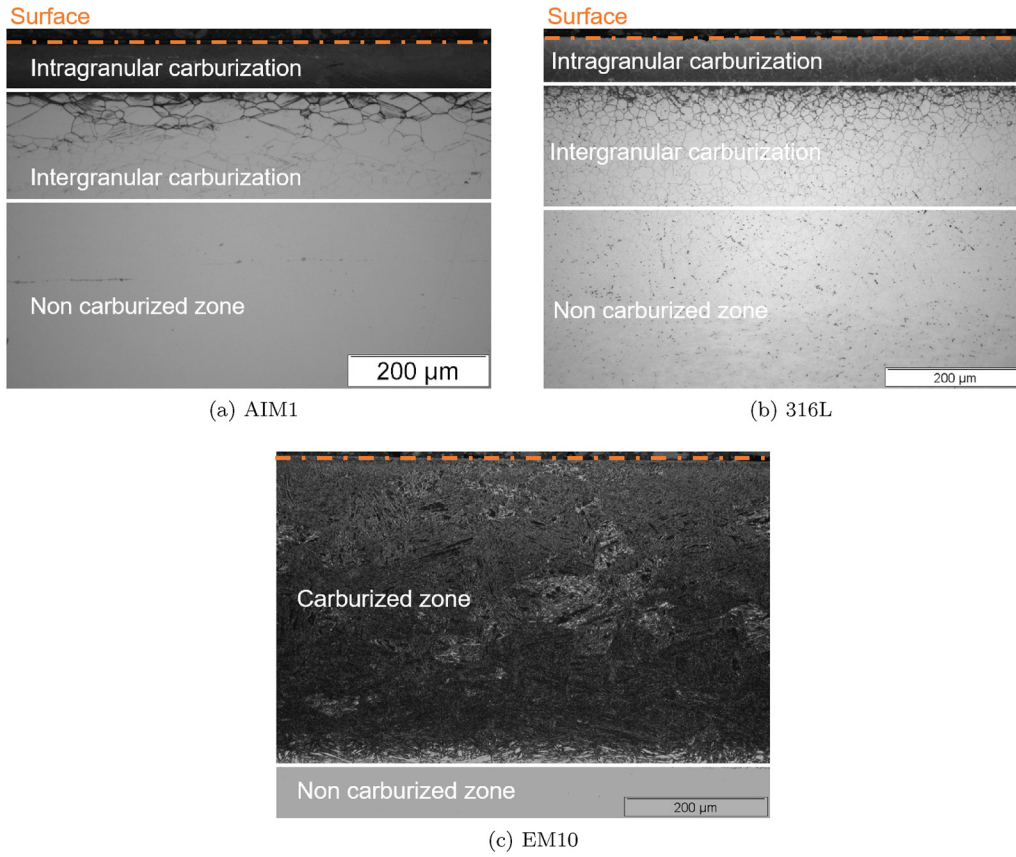


Fig. 2. Microstructure after etching of specimens (a) AIM1, (b) 316L et (c) EM10 after 500 h exposure at 600 °C and  $a_c > 1$ .

### 3. Modelling procedure in DICTRA

The carburization kinetics was simulated with the DICTRA module (database MOBFE3) implemented in the ThermoCalc software (database TCFE8). The *Homogenization model* was used for long-range diffusion occurring in each phase (matrix and carbides here) for which mobility data are available [24,25]. In this model, elemental concentration profiles of all elements are calculated in one dimension. For carbon it is assumed that diffusion occurs only in a matrix which is the austenite or ferrite and that no diffusion occurs through the carbides as no mobility data in the carbides were available in MOBFE3.

In this coupled thermodynamic-kinetic approach, the flux  $J_k$  of component  $k$  in the  $z$  direction is given as function of  $x_k$  and  $V_S$ , the mole fraction and volume of substitutional elements only. The effective diffusion flux of carbon  $J_C^{\text{eff}}$  can be written as follow

$$J_C^{\text{eff}} = -\frac{1}{V_S} f^q M_C^{\text{tot}} x_C^{\text{tot}} \frac{\partial \mu_C}{\partial z} \quad (1)$$

where,

$$x_k^{\text{tot}'} = x_k^{\text{tot}} + f(x_k' - x_k) \quad (2)$$

- $x_k^{\text{tot}'}$ , total mole fraction of  $k$  after the diffusion step;
- $x_k^{\text{tot}}$ , total mole fraction of  $k$  before the diffusion step;
- $x_k'$ , mole fraction of  $k$  in the matrix after the diffusion step;
- $x_k$ , mole fraction of  $k$  in the matrix before the diffusion step;
- $f$ , volume fraction of matrix.

The product  $M_C^{\text{tot}} x_C^{\text{tot}}$  corresponds to the average mobility and composition of carbon and  $\mu_C$  refers to the chemical potential of carbon. The function  $f^q$  (with  $f$  the volume fraction of the matrix and  $q$  a number), is

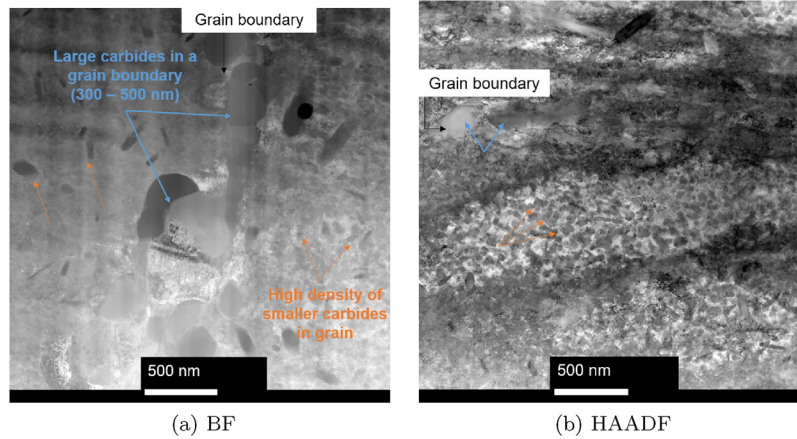


Fig. 3. (a) BF and (b) HAADF images of carbides in grain and grain boundaries at 50  $\mu\text{m}$  from the surface of AIM1 steel after 1000 h exposure at 600  $^{\circ}\text{C}$  and  $a_c > 1$ .

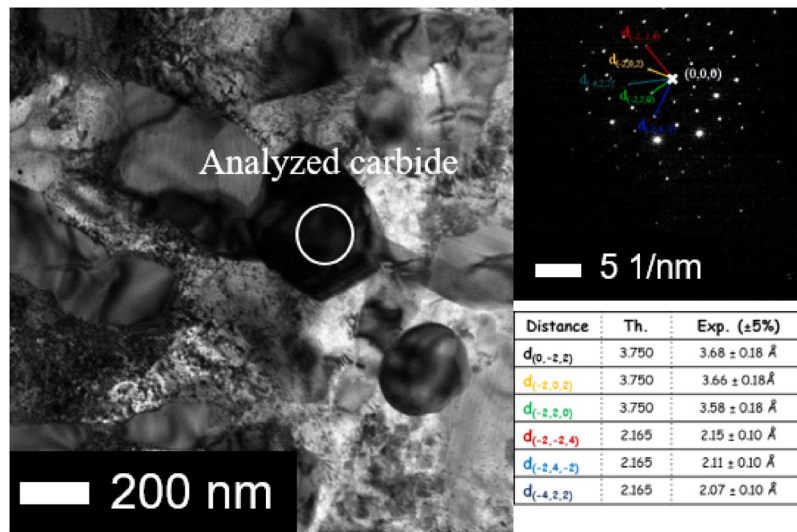


Fig. 4. BF image and diffraction pattern of one carbide located in a grain boundary of AIM1 steel after 5000 h exposure at 600  $^{\circ}\text{C}$  and  $a_c > 1$ .

called the labyrinth factor and, is implemented in the software. This function is used to consider that the presence and the geometry of carbides can modify the diffusion of carbon in the matrix. In carburization studies, the value of  $q$  is usually set at 2 [10–14]. In other studies,  $f^q$ , with  $q$  equal to 1 [26] or 2 [27] was used to simulate the effect of volume fraction binder on the sintering of carbides.

The sample geometry was discretized into a suitable number of volume cells. In the present work, the following phases considered for the calculations were  $\gamma$ -FCC or  $\alpha$ -BCC,  $M_7C_3$  and  $M_{23}C_6$ . As graphite and cementite were not observed experimentally, their formation was prevented (dormant phases). This allowed to obtain a carbon activity greater than 1 at the surface of the steels. For durations up to 3000 h, the carbon concentrations measured by EPMA at the surface of the thick samples were used as boundary conditions at the sodium - metal interface (3.5, 4.0 and 2.7 wt. % for AIM1, 316L and EM10 respectively). These values were equal to their respective homogeneous carbon concentration measured in the foils. For 5000 h exposure, boundaries values equal to 3.7, 4.3 and 2.7 wt. % were used for AIM1, 316L and EM10 steels. The assumption of symmetry at the center of the samples provided the second spatial boundary condition of zero flux for all elements. The measured chemical compositions of the steels in the as-received state were used as the initial composition at time  $t = 0$ . The model provided element concentrations in the matrix ( $\gamma$ -FCC phase for AIM1 and 316L steels or  $\alpha$ -BCC phase for EM10 steel), average element concentrations in all phases and phase fractions as a function of time

and distance.

## 4. Results and discussion

### 4.1. Exposure at 600 and 650 $^{\circ}\text{C}$

For both austenitic steels, three carburized zones were observed after 500 h exposure at 600  $^{\circ}\text{C}$  (Fig. 2). The outer dark zone (called intragranular carburization zone) was composed of a dense precipitation of carbides in grains and at grain boundaries as shown on the TEM images in Fig. 3. This dense precipitation could explain why these areas of the specimen were strongly revealed by the etching (zone entirely dark in Fig. 2). The carbides were enriched in Cr and Fe and some of them were identified as  $M_{23}C_6$  carbides by diffraction TEM as shown in Fig. 4. The presence of graphite or cementite at the surface of the steel could not be identified by TEM analyses. Underneath this first zone, the grains were partially revealed but all grain boundaries were etched (Fig. 2). Finally, this second zone was followed by grain boundaries strongly marked by etching suggesting the precipitation of carbides in grain boundaries. For the ferritic EM10 steel, one single carburized zone was observed in Fig. 2 (intragranular carburization zone). Similar carburized zones were observed at 650  $^{\circ}\text{C}$  (not shown here).

Micrographs and TEM observations did not provide enough information about the nature and the volume fractions of carbides within the depth of the steels. For this purpose, the Rietveld refinements of the

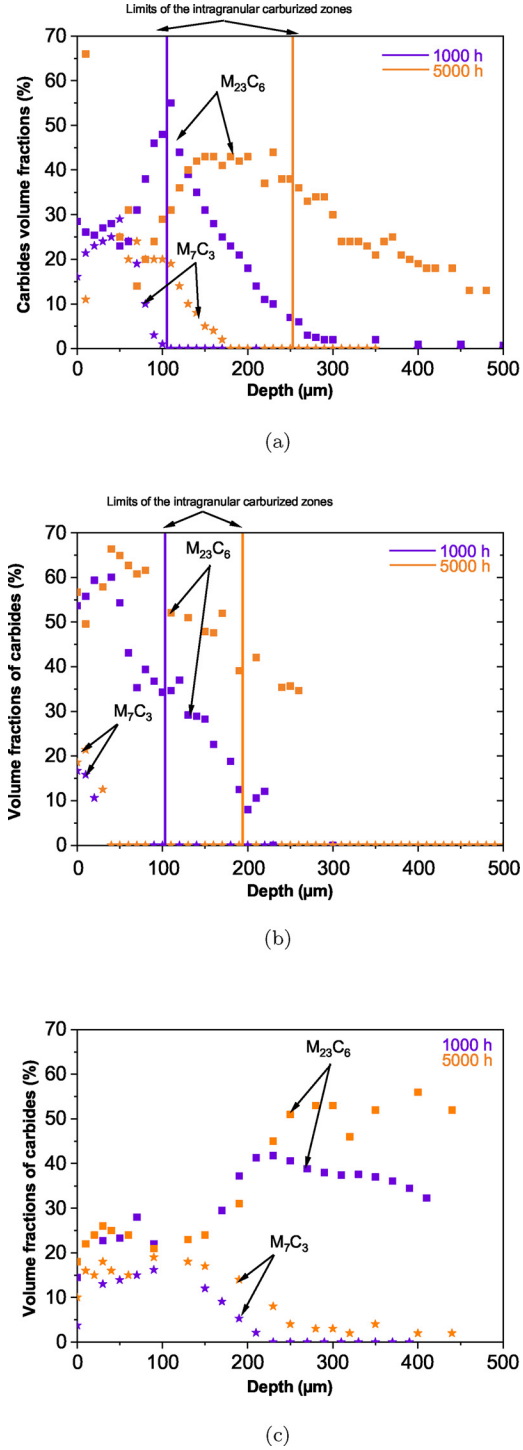


Fig. 5. Carbide volume fractions in (a) AIM1, (b) 316L and (c) EM10 steels after 1000 and 5000 h exposure at 600 °C and  $a_c > 1$ .

diffraction patterns, obtained every 10  $\mu\text{m}$  with transmission XRD, were analyzed. The results are presented in Fig. 5, for the three studied steels. For each diffraction pattern the following parameters were adjusted one at a time and always in the same order: number and type of phases (austenite or ferrite,  $M_{23}C_6$  and  $M_7C_3$ ), lattice parameters, crystallite size and micro strain, the volume fractions of each phase and texture.

The two last parameters are mainly related to the intensities of the peaks and significantly influenced the quality of the Rietveld refinement and thus the calculated volume fractions of carbides. The experimental diffraction patterns did not allow to measure and simulate the

texture of the specimens. In order to correctly predict the volume fractions of phases, an arbitrary texture was used in the MAUD software. This procedure achieved a relative deviation of 5% for the volume fractions of carbides for the AIM1 and EM10 steels. For the 316L steel, a significant relative deviation (around 20%) was observed for depths higher than 250  $\mu\text{m}$ . This effect was also observed for a few diffraction patterns of AIM1 and EM10 steels, where carbides could be identified but not quantified. This observation was due to the low number of peaks. The broadening of the peaks was induced by the small size of the crystallites or an increase of microstrain inside the crystallites. As a consequence, for the 316L steel, the volume fractions of carbides were not reported at depths higher than 250  $\mu\text{m}$ . For AIM1 and EM10 steels, only reliable values of the volume fraction of carbides, extracted from the diffraction patterns, were reported. Examples of diffraction patterns used to obtain the aforementioned results are reported in Fig. 6 for each alloy. These diffraction patterns were obtained at 40  $\mu\text{m}$  from the surface. Initial diffraction patterns and after 5000 h exposure at 600 °C are superimposed.

After exposure,  $M_7C_3$  and  $M_{23}C_6$  carbides (with  $M = \text{Fe, Cr}$ ) were identified in the first 50  $\mu\text{m}$ . In agreement with the TEM measurements, neither graphite nor cementite was found. According to the Rietveld refinements in Fig. 5, large volume fractions of carbides ( $M_7C_3 + M_{23}C_6$ ) were measured, around 50, 80 and 40% at 10  $\mu\text{m}$  depth for AIM1, 316L and EM10 respectively. These values were in agreement with the high density of carbides observed on the TEM images. In Fig. 5, the internal precipitation front was observed to progress with time resulting in the deeper precipitation of  $M_{23}C_6$  located at the grain boundaries of the steels revealed on the micrographs.

The precipitates nature and volume fraction slightly differed between the steels. On one hand, for 316L steel, about 20% of  $M_7C_3$  and 50 to 60% of  $M_{23}C_6$  were measured within the first 30  $\mu\text{m}$  with no noticeable evolution between 1000 and 5000 h. On the other hand, for AIM1 steel, slightly higher volume fractions of  $M_7C_3$  were observed over a larger thickness. The thickness increased with time (from 100 to 170  $\mu\text{m}$  between 1000 and 5000 h). Such a large difference in the volume fractions of  $M_{23}C_6$  and  $M_7C_3$  carbides between 316L and AIM1 steel was not predicted by the ThermoCalc calculations (not shown here) as the two steels have rather similar chemical compositions. The larger volume fractions of carbides for AIM1 steel could be induced by the higher density of dislocations formed during its cold-working. These defects in addition to the presence of grain boundaries could have promoted the transformation of  $M_{23}C_6$  into  $M_7C_3$  carbides. For the EM10 steel, much deeper precipitation of  $M_{23}C_6$  and  $M_7C_3$  was measured and again the thickness increased with time (from 150 to 180  $\mu\text{m}$  between 1000 and 5000 h). This observation can be explained by the greater permeability of carbon in ferrite ( $4 \cdot 10^{-12}$  wt. %  $\text{cm}^2 \text{s}^{-1}$ ) than in austenite ( $5 \cdot 10^{-14}$  and  $9 \cdot 10^{-14}$  wt. %  $\text{cm}^2 \text{s}^{-1}$  for AIM1 and 316L steels respectively) at 600 °C and by its finer microstructure (more grain boundaries acting as diffusion paths).

The difference in the precipitation behavior between the steels was also reflected on the carbon concentration profiles (Fig. 7). In Fig. 7, the measured carbon concentrations were representative of the carbon dissolved in the matrix and the carbon trapped in carbide precipitates. The amount of carbon trapped in the precipitates ( $C^{\text{carbides}}$ ) was calculated using the measured carbide fractions using Eq. (3) [28], with  $\rho^i$  the densities of  $M_7C_3$  and  $M_{23}C_6$  carbides taken from literature [29,30],  $f^i$  the carbide volume fraction from the Rietveld measurements and  $w_C^i$  the weight fraction of carbon in the carbides.

$$C^{\text{carbides}} (\text{wt. \%}) / 100 = \frac{f^{M_{23}C_6} \rho^{M_{23}C_6} w_C^{M_{23}C_6} + f^{M_7C_3} \rho^{M_7C_3} w_C^{M_7C_3}}{f^{M_{23}C_6} \rho^{M_{23}C_6} + f^{M_7C_3} \rho^{M_7C_3}} \quad (3)$$

In Fig. 7, considering the relative deviation of the XRD measurements, a good agreement was observed between the carbon concentration profiles measured by EPMA and the ones calculated with the Rietveld refinement values. This observation suggested that the measured

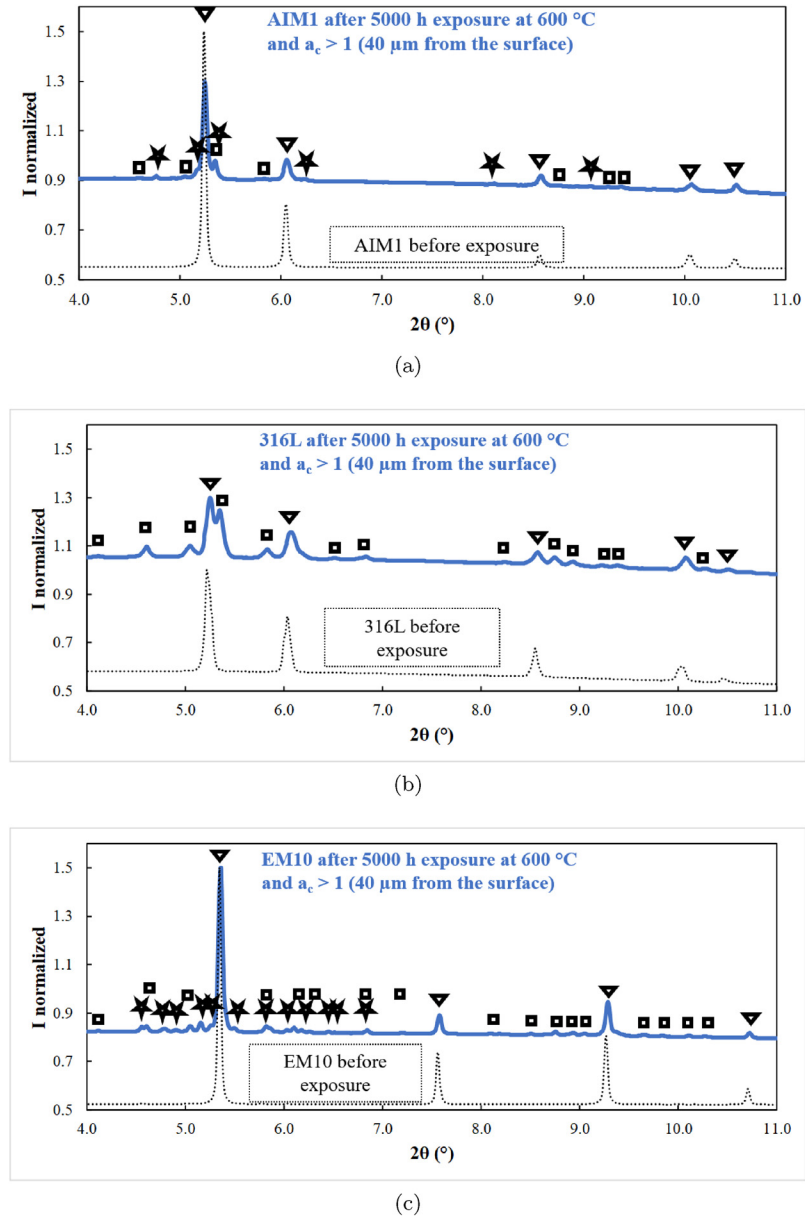


Fig. 6. Diffractogram at 40  $\mu\text{m}$  from the surface of (a) AIM1, (b) 316L and (c) EM10 steels after 5000 h exposure at 600  $^{\circ}\text{C}$  and  $a_c > 1$  ( $\nabla$  austenite  $\star M_7C_3$   $\square M_{23}C_6$ ) superimposed with the diffractogram before exposure.

carbon concentrations corresponded mainly to carbon trapped in precipitates. At 650  $^{\circ}\text{C}$ , the measured carbon concentrations values were close to the one obtained at 600  $^{\circ}\text{C}$  after 500 h exposure (Fig. 8), suggesting as well a large precipitation of carbides in the grains and at the grain boundaries of the steels. Finally, in Fig. 7, the carbon concentration measured at the surface of the specimens was independent of time and corresponded to the homogeneous carbon concentration measured in the foils. This observation indicated that the carbon activity reached at the liquid-metal interface was, at any time, equal to the carbon activity imposed by the carburizing sodium. As mentioned previously, this value was used as a boundary condition for the DICTRA simulations described further in the article.

Interestingly, after carburization, the lattice parameters of austenite or ferrite (reported in Fig. 9) evolved along the carbon concentration profiles (relative deviation of 0.002  $\text{\AA}$ ). In the intragranular carburization zone, the lattice parameter value was lower than the lattice parameter value measured before the experiment. Then, the value increased within the intermediate carburization zone (intra and intergranular

carburization zones) to finally reach the initial lattice parameter value deeper in the steel. The evolution of the lattice parameter is usually induced by modifications of the chemical composition and/or by mechanical stresses in the metallic matrix. In this case, the effect of mechanical stresses on the lattice parameter could be neglected because the integration from 2D to 1D of all the positions of the matrix peaks (austenitic or ferritic) were averaged along the Debye-Scherrer rings obtained on the 2D detector of the ID11 beamline. As a consequence, the decrease of the lattice parameters of austenite or ferrite was likely induced by a modification of the chemical composition. From the literature, the concentration of chromium and the concentration of carbon in the matrix can impact the lattice parameter value. The lattice parameter of austenite increases with addition of chromium in austenite [31] and also with carbon in supersaturation in austenite [32,33]. As demonstrated previously (TEM and XRD measurements), the carbon was mainly trapped into carbides. Thus, the carbon concentration in the matrix of the studied steels were relatively low and no strong impact on the lattice parameter is expected. Thus, the evolution of the

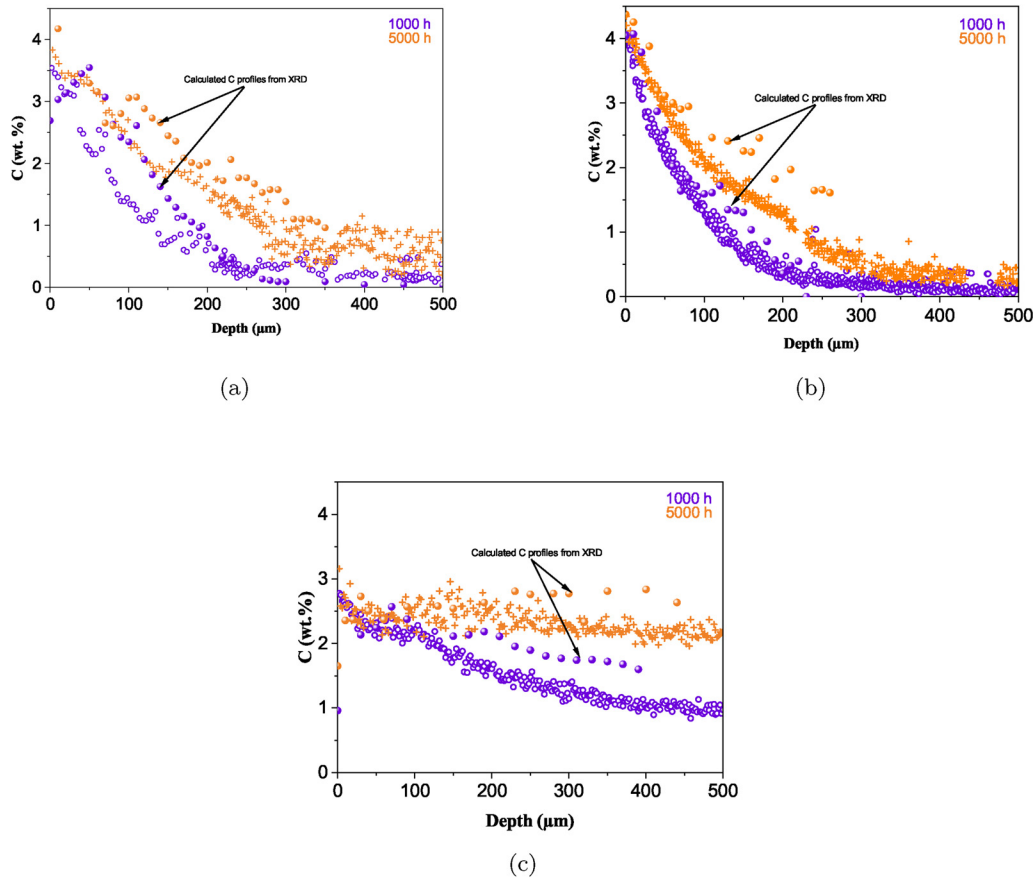


Fig. 7. EPMA carbon concentration profiles of (a) AIM1, (b) 316L and (c) EM10 measured after 1000 and 5000 h exposure at 600 °C and  $a_c > 1$  and calculated carbon concentration profiles from the volume fractions of the carbides measured by XRD.

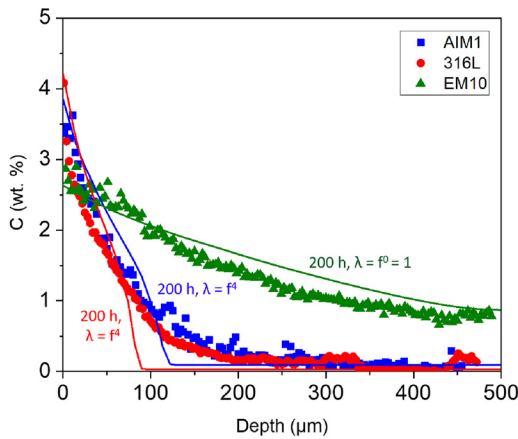


Fig. 8. EPMA carbon concentration profiles (symbols) and DICTRA simulations (lines) and respective labyrinth factors  $f^l$  for AIM1, 316L and EM10 after 200 h exposure at 650 °C and  $a_c > 1$ .

lattice parameter might be rather induced by an evolution of the chromium concentration in the matrix. The following scenario can be proposed. When the chromium carbides were formed, the matrix was depleted in chromium, consequently decreasing the lattice parameter. This decrease was both a function of the degree of chromium enrichment in the carbides and a function of the volume fraction of carbides. In Fig. 9, for AIM1 steel, two “plateau” values were observed. They corresponded to the presence of  $M_7C_3$  and  $M_{23}C_6$  in the zone closer to the surface and then to the presence of  $M_{23}C_6$  underneath. A higher lattice parameter value was observed in the first zone, near the surface,

in good agreement with a higher iron enrichment of carbides (lower chromium depletion) where the carbon activity/concentration is higher (see Fig. 10). Deeper in the steel, the volume fraction of  $M_7C_3$  started to decrease while the volume fraction of  $M_{23}C_6$  increased. This resulted in a higher chromium depletion in the substrate, since the  $M_{23}C_6$  carbides were richer in metallic elements than  $M_7C_3$  (the total carbide volume fraction was roughly the same). This can explain the observed larger decrease of the lattice parameter (2nd “plateau”). Finally, at the end of the intragranular carburization zone, the carbide volume fraction decreased. The extent of chromium depletion decreased and the lattice parameter increased again to reach a value close to the initial lattice parameter value. For 316L steel, the two “plateau” were less pronounced due the lower volume fraction of  $M_7C_3$ . For EM10, the lattice parameter was lower than the initial value through the whole sample thickness as the sample was carburized entirely.

#### 4.2. Thermodynamic and kinetic modeling of carbon diffusion

After thoroughly investigating the extent of carburization in the three steels, numerical simulations were performed to discuss the mechanisms which control the nature and kinetics of carburization.

##### 4.2.1. Influence of grain boundary diffusion and carbides geometry on the carburization kinetics

In the simulations, both carbides  $M_{23}C_6$  and  $M_7C_3$  were considered to be stable. As graphite and cementite were not observed experimentally, their formation was prevented (dormant phases). A comparison of the temporal evolution of the carbon concentration profiles is presented in Fig. 11 for the three steels after 500 and 3000 h exposure at 600 °C. For the austenitic steels in Fig. 11a and b, the experimental carbon profile could not be simulated entirely. As a consequence, the carbon

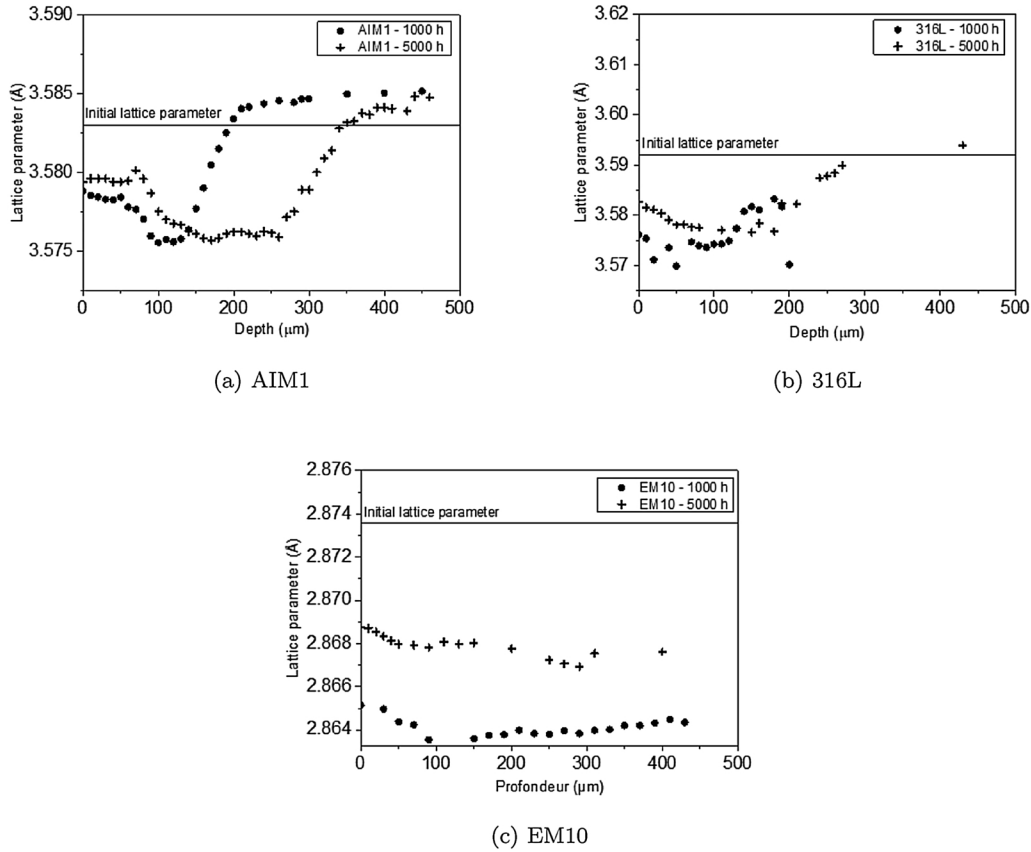


Fig. 9. Evolution of the crystal parameter of (a) AIM1, (b) 316L and (c) EM10 steel as a function of time and depth after 1000 and 5000 h exposure at 600 °C and  $a_c > 1$ .

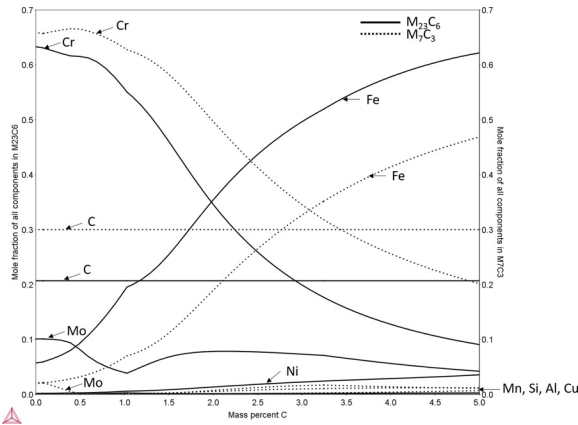


Fig. 10. Evolution of the composition of carbides as function of the total carbon concentration in the steel. Calculated with ThermoCalc at 600 °C with TCFES database and AIM1 steel composition.

concentration profile was divided in two parts: the intragranular and intergranular carburization zones. In the intragranular carburization zone, a good agreement between the predicted and the measured carbon profile was obtained. Nevertheless, this agreement strongly depended on the chosen  $q$  value for the labyrinth factor,  $f^q$ . In Fig. 11a and b, it was not possible to simulate the carbon concentration profiles that corresponded to the intragranular zone with the commonly used labyrinth factor (neither  $f^1$  or  $f^2$  as in the literature [10–14,27,26] nor without one ( $f^0 = 1$ )). The most accurate simulations were achieved with labyrinth factors equal to  $f^4$  after 500 h and  $f^5$  after 3000 h exposure. For the ferritic steel EM10 (Fig. 11c), the values were lower and equal to  $f^2$  after 500 h and between  $f^2$  and  $f^3$  after 3000 h. All the

exponents of the labyrinth factor values were greater than the ones used in the literature ( $f^1$  or  $f^2$  [10–14,27,26]). Furthermore, for the three steels, the  $q$  value increased with the exposure time. This observation suggested a progressive decrease of the diffusion rate of carbon which can be linked to the decrease of the matrix volume fraction (increase of the carbide volume fractions) and to the evolution of the carbide geometry. An evolution of the morphology of the carbides into a more complex and blocking geometry, such as platelets perpendicular to the inwards flux of carbon, could explain a decrease in the carbon diffusion in the alloy. This evolution could not be clearly observed on the etched cross-sections.

At 650 °C, the simulations are superimposed to the carbon concentration profiles in Fig. 8 after 200 h exposure. Again, the labyrinth factors were adjusted in order to fit correctly the intragranular carburization zone. For the austenitic steels, a factor equal to  $f^4$  was used whereas no labyrinth factor was necessary for the ferritic steel EM10 ( $f^0$ ).

Finally, the experimental intergranular carburization zone could not be simulated with the DICTRA model. The disagreement between the experimental and simulated carbon concentration profiles in this zone was clearly visible for the two austenitic steels in Figs. 8 and 11. For these steels, the transition from the intragranular to the intergranular carburization zone was marked by the presence of a carbon diffusion tail deep in the substrate. For the ferritic steel EM10, the effect of grain boundary diffusion was marked after 500 h and no longer visible after 3000 h, where only one “mixed” carburized zone was observed experimentally. As a consequence, the whole carbon concentration profile observed after 3000 h could be simulated with the model with an adjusted labyrinth factor value. The absence of simulated carbon concentration profile in the intergranular zone was of course expected since the diffusion at grain boundaries was not considered in the model used

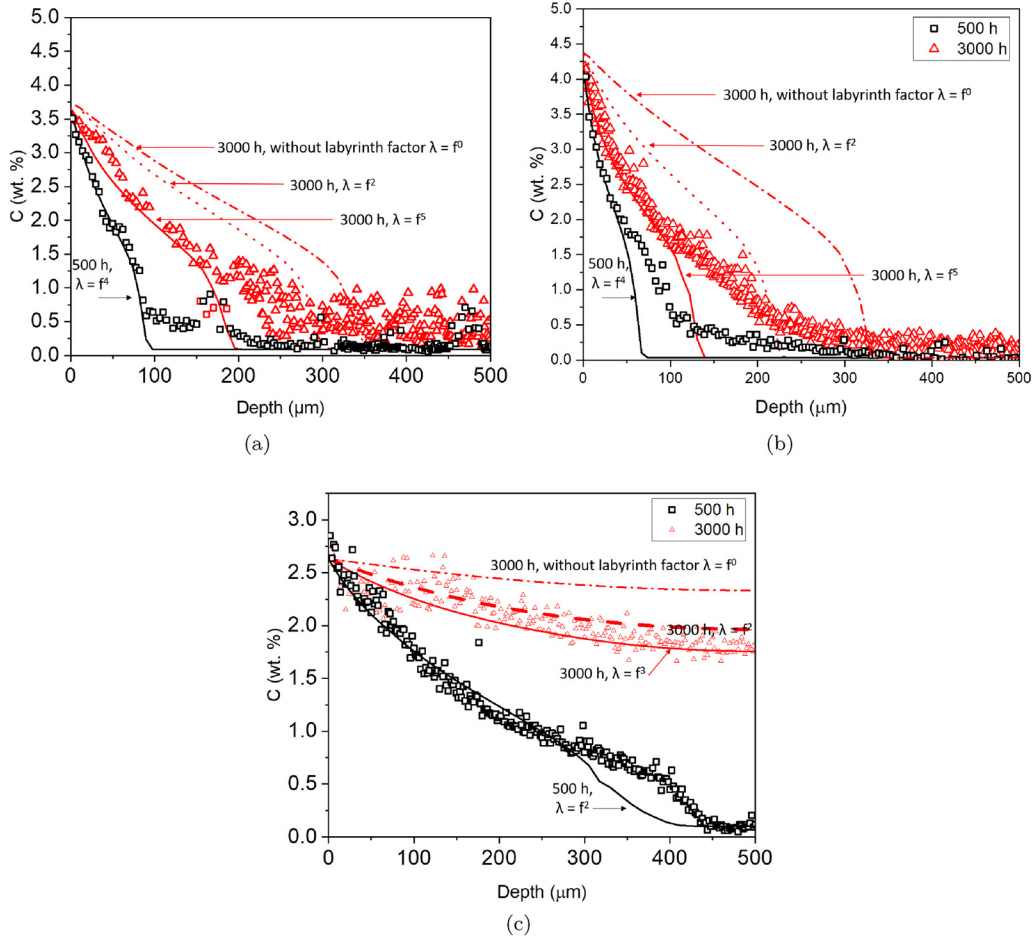


Fig. 11. EPMA carbon concentration profiles (symbols) and DICTRA simulations (lines) with different labyrinth factors  $f^l$  for (a) AIM1, (b) 316L and (c) EM10 steels after 500 and 3000 h exposure at 600 °C and  $a_C > 1$ .

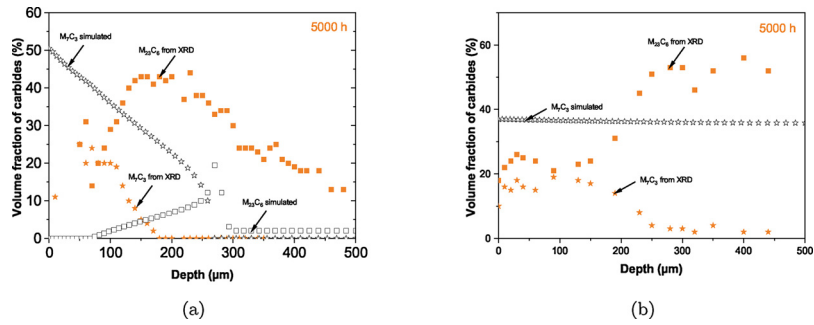


Fig. 12. Experimental and simulated volume fraction of carbides measured in (a) AIM1 and (b) EM10 steels after 5000 h exposure at 600 °C and  $a_C > 1$ .

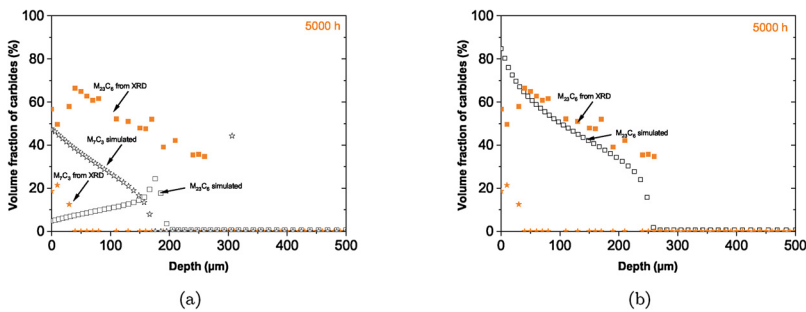


Fig. 13. (a) Experimental and simulated volume fraction of carbides measured in 316L steel after 5000 h exposure at 600 °C and  $a_C > 1$  considering the precipitation of  $M_{23}C_6$  and  $M_7C_3$ . (b) Experimental and simulated volume fraction of carbides measured in 316L steel after 5000 h exposure at 600 °C and  $a_C > 1$  considering the precipitation of  $M_{23}C_6$  only  $f^2$  as labyrinth factor.

**Table 3**Differences between experimental and simulated carbide fraction profiles after 5000 h carburization at 600 °C and  $a_C > 1$ .

Zones	XRD experimental results	Simulations
Zone 1	Presence of $M_7C_3$ and $M_{23}C_6$ with almost constant volume fractions	Presence of $M_7C_3$ of decreasing volume fraction and $M_{23}C_6$ of increasing volume fraction (for AIM1 and 316L only)
Zone 2	Presence of $M_7C_3$ of decreasing volume fraction and $M_{23}C_6$ of increasing volume fraction	Rapid decrease of the volume fraction of $M_{23}C_6$
Zone 3	Slow decrease of the volume fraction of $M_{23}C_6$	Not predicted

in this study. The model used underestimated of the carburization depths reached in the steels. The predicted carburization depths were about 2 times lower than the one measured experimentally for the austenitic steels and 1.5 times lower for the ferritic steel after 500 h exposure.

#### 4.2.2. Non-equilibrium carburization state

In order to understand why higher values of  $q$  were needed for  $f^l$  in our study, compared to the ones usually used in published simulation of carburization kinetics, the experimental and simulated volume fractions of carbides formed in the steels grades were compared. The results are plotted in Figs. 12 and 13a. Two distinct zones were observed on the simulated profiles whereas three different zones were identified on the experimental results. The results are summarized in Table 3.

The last zone in the experimental carbon profile corresponded to the intergranular carburization. As mentioned previously, this zone could not be predicted by the model. Regarding the intragranular carburization zone (zone 1 and 2 in Table 3), the amounts and type of carbides predicted by the DICTRA simulations were different than the one measured experimentally. For the austenitic steels (AIM1 in Fig. 12 and 316L in Fig. 13a), the simulations predicted a large amount of  $M_7C_3$  and a small amount of  $M_{23}C_6$  within the first 200  $\mu\text{m}$ . These predictions differed strongly with the experimental results. Indeed, a large volume fraction of  $M_{23}C_6$  carbides and a smaller volume fraction of  $M_7C_3$  was observed. For EM10 steel, both  $M_7C_3$  and  $M_{23}C_6$  carbides were formed over 200  $\mu\text{m}$  whereas DICTRA only predicted the precipitation of  $M_7C_3$  in the whole thickness of the EM10 steel. Both comparisons indicated that thermodynamic equilibrium of precipitation was not reached in the steels. At 600 °C, the conversion of  $M_{23}C_6$  into  $M_7C_3$  might have been not fast enough to reach thermodynamic equilibrium. As a consequence, the volume fraction of  $M_{23}C_6$  and  $M_7C_3$  carbides could not be precisely predicted with DICTRA. In this model the reactions of formation of carbides are assumed to be fast enough to be at thermodynamic equilibrium. With the aim of predicting correctly the nature and amount of carbides precipitated in the steels, new simulations were performed for the carburization of 316L steel. Only the precipitation of  $M_{23}C_6$  carbides was considered since their volume fraction was larger than the volume fraction of  $M_7C_3$  (the formation of  $M_7C_3$  was prevented, dormant phase). This assumption was relevant for the 316L steel for which a very low amount of  $M_7C_3$  was observed experimentally.

In Fig. 13b, a good agreement between the simulated and experimental carbide fractions was observed, except within the first 10  $\mu\text{m}$  where a non-negligible volume fraction of  $M_7C_3$  carbides was observed experimentally. It is important to mention that, for the DICTRA simulations shown in Fig. 13b, a new labyrinth factor equal to  $f^l$  (which differs from the previously used  $f^l$  considering both carbides  $M_7C_3$  and  $M_{23}C_6$ ) was needed in order to fit correctly the EPMA carbon concentration profiles. This new labyrinth factor value is now similar to values of the common labyrinth factors used in the literature [10–14,27,26].

#### 4.3. Conclusions

The extent of carburization of three different steels exposed in liquid sodium at 600 and 650 °C up to 5000 h was thoroughly characterized.

Precipitation of  $M_{23}C_6$  and  $M_7C_3$  was identified with the use of transmission XRD and TEM in the grains and at grain boundaries of the steels. The larger amount of  $M_7C_3$  observed in the AIM1 steel (strain-hardened) than in the 316L steel (annealed) was associated with a higher density of dislocations. These defects, in addition to the presence of grain boundaries, could have allowed a faster conversion of  $M_{23}C_6$  into  $M_7C_3$  carbides. The deeper precipitation of carbides observed in the EM10 steel was induced by its fine microstructure and the higher solubility product compared to the austenite.

At 600 and 650 °C, several attempts were made to simulate the entire experimental carburization profiles obtained via EPMA measurements in the thickness of the three different steels with DICTRA. Firstly, the simulated carbon profiles strongly underestimated the maximum carburization depths. Half of the carbon concentration profiles measured was induced by the carbon diffusion and precipitation at grain boundaries. This process could not be considered and simulated with the chosen model. New simulations should be performed with the grain boundary model in DICTRA in order to improve the accuracy of the simulations. Secondly, the carbon concentration profiles in the intragranular zone could be predicted correctly but needed a careful adjustment of two input parameters: the labyrinth factor  $f^l$  and the chosen carbide phases. At these intermediate temperatures, it is clear that local thermodynamic equilibrium, such as predicted by DICTRA, was not reached in the steels. As a consequence, the nature and evolution of the amount of the precipitated carbides could not be predicted with accuracy. In the simulations, for the 316L steel, the declared phases were chosen in accordance with the experimental observations. This indicated that the rate of precipitation of carbides must be considered for correct simulations which is, currently, not possible with the DICTRA model.

Unfortunately, even if a more accurate description of the phases could be used for one specimen, the value of  $f^l$  could not be determined experimentally. As a consequence, the value was adjusted to the experimental profiles. As indicated in the literature [10–14], the role of the labyrinth factor is to decrease the carbon flux in the matrix when the precipitate volume fraction increases. At 600 and 650 °C, the blocking effect of the carbides could not be neglected and was observed to evolve with time. Thus, the description of the labyrinth factor in the model should be improved. For example, by considering the evolution of the morphology of carbides with time.

#### Acknowledgements

The authors are grateful to the ID11 beamline team: Pavel Sedmak and Jonathan Wright (ESRF Grenoble, France) for their assistance in carrying out the XRD experiments. Prof. Daniel Chateigner (CRISMAT, Caen, France) is gratefully acknowledged for his help with the MAUD software and Rietveld analyses. Authors are also thankful to Rishi Pillai (ORNL, United States) for his advice with the DICTRA simulations.

#### References

- [1] J.P. Hugot, Prolongation de la durée de vie des EA de la filière N.R. Bilan des examens réalisés sur les gaines en 316Ti hypereffort et 1515Ti écroui., Note Technique CEA: DECM/SRMA 99-2330 ind. 0, DR. (1999).
- [2] W. Anderson, G. Sneesby, Carburization of austenitic stainless steel in liquid sodium, Atomic International Report NAASR – 5289, (1960).

- [3] J.R. Gwyther, M.R. Hobdell, A.J. Hooper, Carburization of austenitic and ferritic alloys in carbon-saturated sodium at 916 K, *Metals Technol.* 1 (1) (1974) 406–411, <https://doi.org/10.1179/030716974803288220>.
- [4] H. Aubert, M. Champigny, D. Gauvain, L. Meny, M. Pigoury, Carburization d'acier 316 par transfert de carbone dans le sodium, *Note Technique CEA: SRMA/GMAR 78-812*, (1978).
- [5] A. Thorley, M. Hobdell, *Carbon in Sodium – A Review of Work in the UK*, CEGB, Berkeley Nuclear Laboratories, 1984.
- [6] L. Brunel, Proposition d'une loi enveloppe de carburation des gaines d'éléments absorbants, *Note Technique CEA: SDC 84-2014 ind. 0*, (1984).
- [7] J. Dickson, A. Raine, Carburisation of Stainless Steel Immersed in Carbon-Contaminated Sodium: A New Technique for Estimating the Diffusion Coefficients vol. 2, *Liquid Metal Engineering and Technology*, 1988.
- [8] J. Crank, *Mathematics of Diffusion*, Oxford University Press, 1957.
- [9] A. Borgenstam, L. Höglund, J. Ågren, A. Engström, Dictra, a tool for simulation of diffusional transformations in alloys, *J. Phase Equilibria* 21 (3) (2000) 269, <https://doi.org/10.1361/105497100770340057>.
- [10] A. Engström, L. Höglund, J. Ågren, Computer simulation of diffusion in multiphase systems, *Metall. Mater. Trans. A* 25 (6) (1994) 1127–1134, <https://doi.org/10.1007/BF02652288>.
- [11] T. Turpin, J. Dulcy, M. Gantois, Carbon diffusion and phase transformations during gas carburizing of high-alloyed stainless steels: Experimental study and theoretical modeling, *Metall. Mater. Trans. A* 36 (10) (2005) 2751–2760, <https://doi.org/10.1007/s11661-005-0271-4>.
- [12] C. Sudha, N.S. Bharasi, R. Anand, H. Shaikh, R. Dayal, M. Vijayalakshmi, Carburization behavior of aisi 316ln austenitic stainless steel – experimental studies and modeling, *J. Nucl. Mater.* 402 (2) (2010) 186–195, <https://doi.org/10.1016/j.jnucmat.2010.05.023> <http://www.sciencedirect.com/science/article/pii/S0022311510002357>.
- [13] J. Garcia, O. Prat, Experimental investigations and dictra simulations on formation of diffusion-controlled fcc-rich surface layers on cemented carbides, *Appl. Surf. Sci.* 257 (21) (2011) 8894–8900, <https://doi.org/10.1016/j.apsusc.2011.05.024> <http://www.sciencedirect.com/science/article/pii/S0169433211007148>.
- [14] D. Rong, J. Gong, Y. Jiang, Thermodynamic simulation of low temperature colossal carburization of austenitic stainless steel, *Proc. Eng.* 130 (2015) 676–684, <https://doi.org/10.1016/j.proeng.2015.12.296> <http://www.sciencedirect.com/science/article/pii/S1877705815041806>.
- [15] K. Bongartz, R. Schulten, W.J. Quadackers, H. Nickel, A finite difference model describing carburization in high-temperature alloys, *CORROSION* 42 (7) (1986) 390–397, <https://doi.org/10.5006/1.3584919>.
- [16] K. Bongartz, W.J. Quadackers, R. Schulten, H. Nickel, A mathematical model describing carburization in multielement alloy systems, *Metall. Trans. A* 20 (6) (1989) 1021–1028, <https://doi.org/10.1007/BF02650138>.
- [17] H.J. Grabke, U. Gravenhorst, W. Steinkusch, Aufkohlung von chrom-nickel-eisenstählen in der kohlenstoffpackung, *Mater. Corros.* 27 (5) (1976) 291–296, <https://doi.org/10.1002/maco.19760270502>.
- [18] G.K. Johnson, E.H.V. Deventer, J.P. Ackerman, W.N. Hubbard, D.W. Osborne, H.E. Flotow, Enthalpy of formation of disodium acetylide and of monosodium acetylide at 298.15 k, heat capacity of disodium acetylide from 5 to 350 k, and some derived thermodynamic properties, *J. Chem. Thermodyn.* 5 (1) (1973) 57–71, [https://doi.org/10.1016/S0021-9614\(73\)80063-1](https://doi.org/10.1016/S0021-9614(73)80063-1) <http://www.sciencedirect.com/science/article/pii/S0021961473800631>.
- [19] R. Ainsley, L.P. Hartlib, P. Holroyd, G. Long, The solubility of carbon in sodium, *J. Nucl. Mater.* 52 (2) (1974) 255–276, [https://doi.org/10.1016/0022-3115\(74\)90172-X](https://doi.org/10.1016/0022-3115(74)90172-X).
- [20] M. Romedenne, F. Rouillard, B. Duprey, D. Hamon, M. Tabarant, D. Monceau, Carburization of austenitic and ferritic steels in carbon-saturated sodium: preliminary results on the diffusion coefficient of carbon at 873 k, *Oxid. Metals* 87 (5) (2017) 643–653, <https://doi.org/10.1007/s11085-017-9733-5>.
- [21] N. Vaxelaire, P. Gergaud, G.B.M. Vaughan, Sub-micrometre depth-gradient measurements of phase, strain and texture in polycrystalline thin films: a nano-pencil beam diffraction approach, *J. Appl. Crystallogr.* 47 (2) (2014) 495–504, <https://doi.org/10.1107/S1600576714000557>.
- [22] J. Baillieux, D. Poquillon, B. Malard, Observation using synchrotron x-ray diffraction of the crystallographic evolution of alpha-titanium after oxygen diffusion, *Philos. Mag. Lett.* 95 (5) (2015) 245–252, <https://doi.org/10.1080/09500839.2015.1014876>.
- [23] L. Lutterotti, R. Vasin, H. Wenk, Rietveld texture analysis from synchrotron diffraction images. I. Calibration and basic analysis, *Powder Diffr.* 29 (1) (2014) 76–84, <https://doi.org/10.1017/S0885715613001346>.
- [24] H. Larsson, A. Engström, A homogenization approach to diffusion simulations applied to  $\alpha + \gamma$  Fe-Cr-Ni diffusion couples, *Acta Mater.* 54 (9) (2006) 2431–2439, <https://doi.org/10.1016/j.actamat.2006.01.020> <http://www.sciencedirect.com/science/article/pii/S1359645406000954>.
- [25] H. Larsson, L. Höglund, Multiphase diffusion simulations in 1D using the dictra homogenization model, *Calphad* 33 (3) (2009) 495–501, <https://doi.org/10.1016/j.calphad.2009.06.004> <http://www.sciencedirect.com/science/article/pii/S0364591609000522>.
- [26] R. Frykholm, M. Ekroth, B. Jansson, J. Ågren, H.-O. Andrén, A new labyrinth factor for modelling the effect of binder volume fraction on gradient sintering of cemented carbides, *Acta Mater.* 51 (4) (2003) 1115–1121, [https://doi.org/10.1016/S1359-6454\(02\)00515-3](https://doi.org/10.1016/S1359-6454(02)00515-3) <http://www.sciencedirect.com/science/article/pii/S1359645402005153>.
- [27] M. Ekroth, R. Frykholm, M. Lindholm, H.-O. Andrén, J. Ågren, Gradient zones in w-c-ti(c,n)-co-based cemented carbides: experimental study and computer simulations, *Acta Mater.* 48 (9) (2000) 2177–2185, [https://doi.org/10.1016/S1359-6454\(00\)00029-X](https://doi.org/10.1016/S1359-6454(00)00029-X) <http://www.sciencedirect.com/science/article/pii/S135964540000029X>.
- [28] R. Pillai, A. Chyrkin, D. Grüner, W. Nowak, N. Zheng, A. Kliewe, W. Quadackers, Carbides in an aluminised single crystal superalloy: tracing the source of carbon, *Surf. Coat. Technol.* 288 (2016) 15–24, <https://doi.org/10.1016/j.surfcoat.2015.12.066> <http://www.sciencedirect.com/science/article/pii/S0257897215304965>.
- [29] W.M. Haynes, *CRC Handbook of Chemistry and Physics*, 95th ed., Taylor and Francis, Boca Raton, FL, 2014 an imprint of CR, Press, description based upon print version of record. <https://www.lib.uts.edu.au/goto?url=http://UTS.ebib.com.au/patron/FullRecord.aspx?p=1591582>.
- [30] W.B. Pearson, *Interstitial Alloys*, H.J. Goldschmidt, Plenum, New York; Butterworths, London, 1968, <https://doi.org/10.1126/science.162.3850.251-a> <http://science.sciencemag.org/content/162/3850/251.2.full.pdf>.
- [31] D. Dyson, B. Holmes, Effect of alloying addition on the lattice parameter of austenite, *J. Iron Steel Inst.* 208 (1970) 469–474.
- [32] Y. Sun, X. Li, T. Bell, Structural characteristics of low temperature plasma carburised austenitic stainless steel, *Mater. Sci. Technol.* 15 (10) (1999) 1171–1178, <https://doi.org/10.1179/026708399101505077>.
- [33] Y. Cao, F. Ernst, G. Michal, Colossal carbon supersaturation in austenitic stainless steels carburized at low temperature, *Acta Mater.* 51 (14) (2003) 4171–4181, [https://doi.org/10.1016/S1359-6454\(03\)00235-0](https://doi.org/10.1016/S1359-6454(03)00235-0) <http://www.sciencedirect.com/science/article/pii/S1359645403002350>.